

Cold molecules formation by shaping with light the short-range interaction between cold atoms: photoassociation with strong laser pulses

Mihaela Vatasescu

Institute of Space Sciences, MG-23, 77125 Bucharest-Magurele, Romania

E-mail: mihaela@venus.nipne.ro

Abstract. The paper investigates cold molecules formation in the photoassociation of two cold atoms by a strong laser pulse applied at short interatomic distances, which lead to a molecular dynamics taking place in the light-induced (adiabatic) potentials. A two electronic states model in the cesium dimer is used to analyse the effects of this strong coupling regime and to show specific results: i) acceleration of the ground state population to the inner zone due to a non-impulsive regime of coupling at short and intermediate interatomic distances; ii) formation of cold molecules in strongly bound levels of the ground state, where the population at the end of the pulse is much bigger than the population photoassociated in bound levels of the excited state; iii) the final momentum distribution of the ground state wavepacket keeping the signatures of the maxima in the initial wavefunction continuum. It is shown that the topology of the light-induced potentials plays an important role in dynamics.

PACS numbers: 31.15.xv, 32.80.Qk, 33.15.Vb, 33.20.Tp, 34.50.Cx

Submitted to: *J. Phys. B: At. Mol. Opt. Phys.*

1. Introduction

Photoassociation of cold atoms as a technique to form cold molecules has known new developments in the last years due to explorations using shaped laser pulses in order to control molecules formation: enhancement in cold molecules production and attainment of deeply bound vibrational states are both desired. The road from cold atoms photoassociation using continuous lasers [1] which keep the selectivity of transitions to the use of ultrashort pulses with broad bandwidth brought the challenges of a new physics. Prospective experiments using shaped femtoseconds laser pulses to photoassociate ultracold atoms [2, 3] have shown the coherence of the process, but emphasized the difficulty to increase the number of created molecules. On the other hand, frequency-chirped light pulses in the nanosecond range were used to coherently control ultracold atomic Rb collisions showing the enhancement of short-range collisional flux [4, 5]. Other experimental developments trying to establish coherent control techniques for cold molecules formation explored multiphoton photoassociative ionization in a Rb magneto-optical trap combining femtoseconds and continuous lasers [6] and optimal control of multiphoton ionization of Rb₂ molecules using femtosecond laser pulses in a closed feedback loop [7]. Theoretical studies of pulsed photoassociation explored a variety of schemas to control cold molecular dynamics: with chirped pulses [8, 9, 10, 11], pump-dump schemes to stabilize the cold molecules [12, 13, 14, 15], schemes using adiabatic passage [16, 17].

The present paper prolongs previous works [18, 19], the aim being to investigate theoretically the photoassociation of two cold atoms by strong laser pulses applied at small or intermediate interatomic distances. Such pulses have to be only “moderately strong” in order to avoid additional processes as ionization, and to act far from the atomic resonance (i.e. with a large red detuning, the colliding atoms being excited at small interatomic separations), to avoid the transfer of population to the continuum of the excited state. This regime of strong coupling and large detuning in cold atoms photoassociation can be used to address some specific interrogations: i) One interest is to explore if a strong pulse applied at small interatomic distances could be used to create strongly bound cold molecules, i.e. if such a pulse could accelerate efficiently the initial population, located at large interatomic distances in a cold collision, towards the inner region. ii) Secondly, a transition taking place at small or intermediate interatomic distances brings a regime necessarily “seeing” the nodal structure of the initial ground state continuum, and then we expect such traces in our results. iii) We are interested to explore the effects produced by a rather strong regime of coupling, generally not easy to be predicted. In [18] we have shown that for a strong coupling, characteristic times related to the adiabatic potentials become relevant in dynamics. The present work will explicitly explore the role played by the topology of the light-induced potentials in the dynamics and the photoassociation results.

Our analysis is pursued on the example of the $a^3\Sigma_u^+(6s, 6s) \rightarrow 1_g(6s, 6p_{3/2})$ transition in Cs₂. The structure of the paper is the following: Section 2 describes the

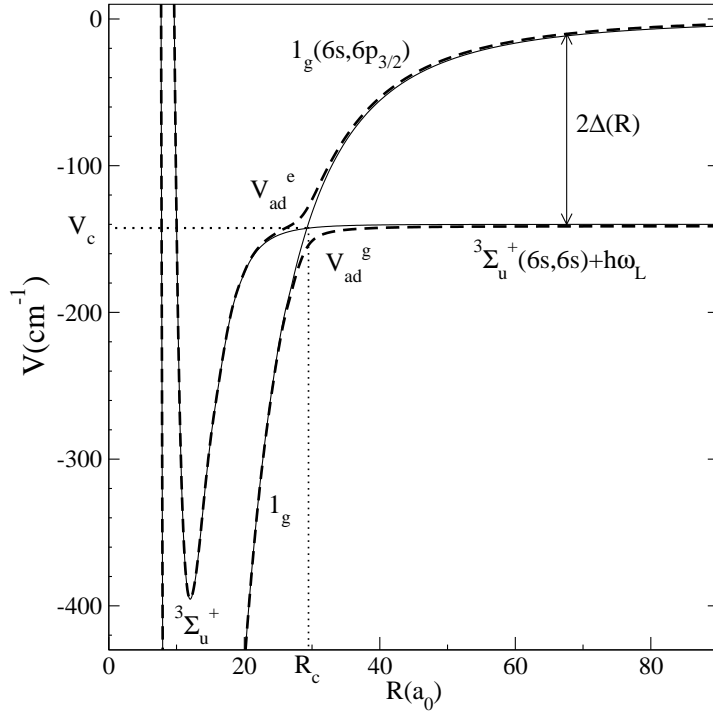


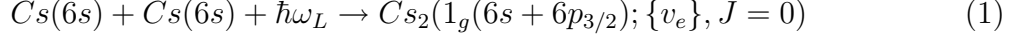
Figure 1. $a^3\Sigma_u^+(6s, 6s)$ and $1_g(6s, 6p_{3/2})$ electronic potentials of Cs_2 (full lines), dressed with the photon of energy $\hbar\omega_L = E_{6p_{3/2}} - E_{6s} - \hbar\Delta_L$ ($\hbar\Delta_L = 140 \text{ cm}^{-1}$) and crossing in $R_c = 29.3 a_0$, $V_c = V_{1_g}(R_c) = V_\Sigma(R_c) = -143 \text{ cm}^{-1}$. Dashed lines: the adiabatic potentials (V_{ad}^e, V_{ad}^g) obtained from the diagonalization of the 2×2 potential matrix (13) with the coupling $W_L = 13.17 \text{ cm}^{-1}$. The energy origin is taken to be the dissociation limit $E_{6s+6p_{3/2}} = 0$ of the $1_g(6s + 6p_{3/2})$ potential.

time-dependent model and the time scales relevant in the photoassociation dynamics, as well as the initial wavefunction and the time evolution of the wavepackets during the pulse. In Section 3 we analyse the population transfer during the pulse and show the relevance of the light-induced potentials for the dynamics. In Section 4 are shown and interpreted the results at the end of the pulse: formation of strongly bound cold molecules in ground and excited electronic states (Section 4.1), acceleration of the ground state population to small interatomic distances (Section 4.2), and the momentum structure of the final wavepacket in the ground state which reflects the maxima of the initial continuum wavefunction (Section 4.3). An Appendix is connected to Section 4.3. Section 5 contains comments and conclusions.

2. Simulation of the photoassociation dynamics during the pulse

The photoassociation reaction is between two cold cesium atoms colliding in the ground state potential $g = a^3\Sigma_u^+(6s, 6s)$, at a temperature $T = 0.11 \text{ mK}$, which are excited by a moderately strong laser pulse (with intensity $I \approx 43 \text{ MW/cm}^2$) to form a molecule in a superposition of vibrational levels $\{v_e\}$ of the excited electronic potential $e = 1_g(6s, 6p_{3/2})$. Only the s wave of the collision is considered. For a rotational

quantum number $J = 0$, the process can be schematized as:



The pulse is red-detuned with $\hbar\Delta_L = 140 \text{ cm}^{-1}$ from the energy $\hbar\omega_{at} = E_{6p_{3/2}} - E_{6s}$ of the D2 atomic transition ($\hbar\omega_L = \hbar\omega_{at} - \hbar\Delta_L$). The large detuning $\hbar\Delta_L$ determines a crossing of the field dressed diabatic potentials at the interatomic distance $R_c = 29.3 \text{ a}_0$, with $V_c = V_{1_g}(R_c) = V_\Sigma(R_c) = -143 \text{ cm}^{-1}$ (figure 1).

The $a^3\Sigma_u^+(6s, 6s)$ and $1_g(6s, 6p_{3/2})$ electronic potentials used in the present calculation (figure 1) are built from quantum chemistry [20] and asymptotic calculations [21, 22] and were described in a previous paper [18].

2.1. Time-dependent model

The dynamics of the photoassociation process is simulated by solving numerically the time-dependent Schrödinger equation associated with the radial motion of the wavepackets $\Psi_{1_g}(R, t)$ and $\Psi_\Sigma(R, t)$ in the electronic channels 1_g and $a^3\Sigma_u^+$, coupled by an electric field with the amplitude $\mathcal{E}(t) = \mathcal{E}_0 f(t) \cos \omega_L t$. The equation can be written as [18]:

$$i\hbar \frac{\partial}{\partial t} \begin{pmatrix} \Psi_{1_g}(R, t) \\ \Psi_\Sigma(R, t) \end{pmatrix} = \begin{pmatrix} \hat{\mathbf{T}} + V_{1_g}(R) & W_L f(t) \\ W_L f(t) & \hat{\mathbf{T}} + V_\Sigma(R) \end{pmatrix} \begin{pmatrix} \Psi_{1_g}(R, t) \\ \Psi_\Sigma(R, t) \end{pmatrix} \quad (2)$$

Equation (2) is obtained in the Born-Oppenheimer approximation for the diatomic molecule and using the rotating wave approximation with the frequency $\omega_L/2\pi$. The potentials $V_{1_g}(R)$ and $V_\Sigma(R)$ are the diabatic electronic potentials crossing in R_c , represented in figure 1. $\hat{\mathbf{T}}$ is the kinetic energy operator and $W_L f(t)$ the coupling between the two channels, with $f(t)$ the temporal envelope of the pulse. $W_L = -\frac{1}{2} \mathcal{E}_0 D_{ge}^{e_L}$, where $\mathcal{E}_0 = \sqrt{\frac{2I}{c\epsilon_0}}$ is the field amplitude (with I the laser intensity), e_L^* the polarization, and $D_{ge}^{e_L}$ the transition dipole moment between the ground and the excited molecular electronic states. We neglect the R-dependence of the transition dipole moment, using the asymptotic value $D_{ge}^{e_L}$ deduced from standard long-range calculations for a linear polarisation vector e_L^* . This approximation remains good for the present calculation, as for distances around the crossing $R_c = 29.3 \text{ a}_0$, the dipole moment is closed to its asymptotic value, $D_{ge}^{e_L}(R_c) \approx 0.9 D_{ge}^{e_L}$, and decreases slowly for smaller distances [23]. For a pulse intensity $I \approx 43 \text{ MW/cm}^2$, the coupling becomes $W_L = 13.17 \text{ cm}^{-1}$, inducing a significant avoided crossing, as it can be seen in figure 1, where the light-induced or adiabatic potentials V_{ad}^e , V_{ad}^g are represented with dashed lines.

The numerical calculations were made for a rectangular pulse with a duration of $\approx 300 \text{ ps}$, whose envelope $f(t)$ is represented in figure 2.

The Schrödinger equation (2) is solved by propagating in time an initial wavefunction $\begin{pmatrix} 0 \\ \Psi_\Sigma(R, 0) \end{pmatrix}$ on a spatial grid with the length $L_R = 760 \text{ a}_0$. The time

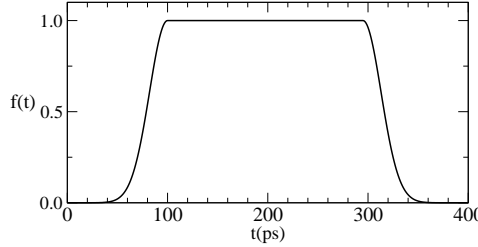


Figure 2. Temporal envelope $f(t)$ of the photoassociating pulse.

propagation uses the Chebychev expansion of the evolution operator [24, 25] and the Mapped Sine Grid (MSG) method [10, 27] to represent the radial dependence of the wavepackets.

The results extracted from the dynamics are:

- the evolution of the wavepackets during the pulse, for the two channels $g = a^3\Sigma_u^+$, $e = 1_g$, in the position representation, $\Psi_{\Sigma,1g}(R, t)$, and momentum representation, defined by the Fourier transforms $\Psi_{\Sigma,1g}(p, t)$;
- the evolution of the population in each electronic state during the pulse. At a given instant t , the population in one of the electronic states g, e is calculated on the spatial grid extending from R_{min} to L_R , as:

$$P_{g,e}(t) = \int_{R_{min}}^{L_R} |\Psi_{g,e}(R', t)|^2 dR' \quad (3)$$

The spatial grid is chosen such as at every instant t the total population is normalized at 1 on the grid ($P_{\Sigma}(t) + P_{1_g}(t) = 1$). At $t=0$ the population is entirely in the ground state ($P_{\Sigma}(0) = 1$).

2.2. Time scales related to the laser coupling and vibrational movement

The time scales relevant for the dynamics are related to the laser coupling and to the vibrational movements in the electronic potentials. The spontaneous emission from the excited state is neglected, as the time evolution of hundreds picoseconds studied here is short compared with the spontaneous emission time of about 30 ns.

We begin by defining the characteristic times connected to the laser coupling.

A *local time-dependent Rabi period* can be associated with the laser coupling $W_L f(t)$ between the two electronic states [9]:

$$T_{Rabi}(R, t) = \frac{\hbar\pi}{\sqrt{(W_L f(t))^2 + \Delta^2(R)}}, \quad (4)$$

where $2\Delta(R) = |V_{1_g}(R) - V_{\Sigma}(R)|$ is the local detuning (see figure 1). Such a characteristic time is relevant if the impulsive approximation remains valid on the whole duration of the pulse, i.e. if the relative motion of the two nuclei can be considered as frozen during the pulse duration.

For the rectangular pulse studied here the coupling remains constant in the time interval (100 ps, 300 ps), so we can refer in the analysis at a *local Rabi period* associated to the constant coupling W_L :

$$T_{Rabi}^L(R) = \frac{\hbar\pi}{\sqrt{W_L^2 + \Delta^2(R)}} \quad (5)$$

This local Rabi period has its maximum at the potentials crossing ($T_{Rabi}^L(R_c) = 1.27$ ps), diminishing with the increasing of the local detuning (for example $T_{Rabi}^L(89 a_0) = 0.24$ ps).

One can also associate a Rabi period with the *beating induced by the coupling W_L between two specific vibrational states*, one belonging to the excited electronic state, and the other to the ground state. Indeed, in equation (2) the wavepackets can be developed as superpositions of vibrational wavefunctions $\{|\chi_{v_e, v_g}(R)\rangle\}$ with eigenenergies E_{v_e, v_g} , corresponding to each electronic Hamiltonian $\hat{\mathbf{H}}_{e,g} = \hat{\mathbf{T}} + \hat{\mathbf{V}}_{e,g}$ ($\hat{\mathbf{H}}_{e,g}|\chi_{v_e, v_g}\rangle = E_{v_e, v_g}|\chi_{v_e, v_g}\rangle$):

$$\Psi_{1g}(R, t) = \sum_{v_e} c_{v_e}(t) \exp\left(-\frac{i}{\hbar} E_{v_e} t\right) \chi_{v_e}(R), \quad (6)$$

$$\Psi_{\Sigma}(R, t) = \sum_{v_g} c_{v_g}(t) \exp\left(-\frac{i}{\hbar} E_{v_g} t\right) \chi_{v_g}(R), \quad (7)$$

Supposing only two vibrational states, $c_{v_e}(t) \exp\left(-\frac{i}{\hbar} E_{v_e} t\right) \chi_{v_e}(R)$ and $c_{v_g}(t) \exp\left(-\frac{i}{\hbar} E_{v_g} t\right) \chi_{v_g}(R)$, respectively, with $|c_{v_e}(t)|^2 + |c_{v_g}(t)|^2 = 1$, $|c_{v_g}(0)|^2 = 1$, $|c_{v_e}(0)|^2 = 0$, which are coupled by W_L in equation (2), one obtains for the oscillating population in the excited state:

$$|c_{v_e}(t)|^2 = \frac{|W_L \langle \chi_{v_e} | \chi_{v_g} \rangle|^2}{(\hbar \Omega_{v_e, v_g})^2} \sin^2(\Omega_{v_e, v_g} t), \quad (8)$$

$$\hbar \Omega_{v_e, v_g} = \sqrt{|W_L \langle \chi_{v_e} | \chi_{v_g} \rangle|^2 + [(E_{v_e} - E_{v_g})/2]^2}. \quad (9)$$

The corresponding Rabi period will depend on the overlap $\langle \chi_{v_e} | \chi_{v_g} \rangle$ of the vibrational functions:

$$T_{v_e, v_g}^L = \frac{\pi}{\Omega_{v_e, v_g}} \quad (10)$$

The time scale associated with the *vibrational motion* of a vibrational level v with binding energy E_v in an electronic potential is:

$$T_v^{vib} = \frac{2\pi\hbar}{|E_{v+1} - E_v|}. \quad (11)$$

To estimate the coupling influence on the dynamics, the time scales (5) and (10) associated with the laser coupling shall be compared with the vibrational periods (11) of levels in the ground and excited potentials. In the case treated here, the Rabi periods associated with the laser coupling are of the order of picosecond, being much smaller than the characteristic vibrational periods implied in the problem (tens or hundred ps), which indicates a case of *strong coupling* [18].

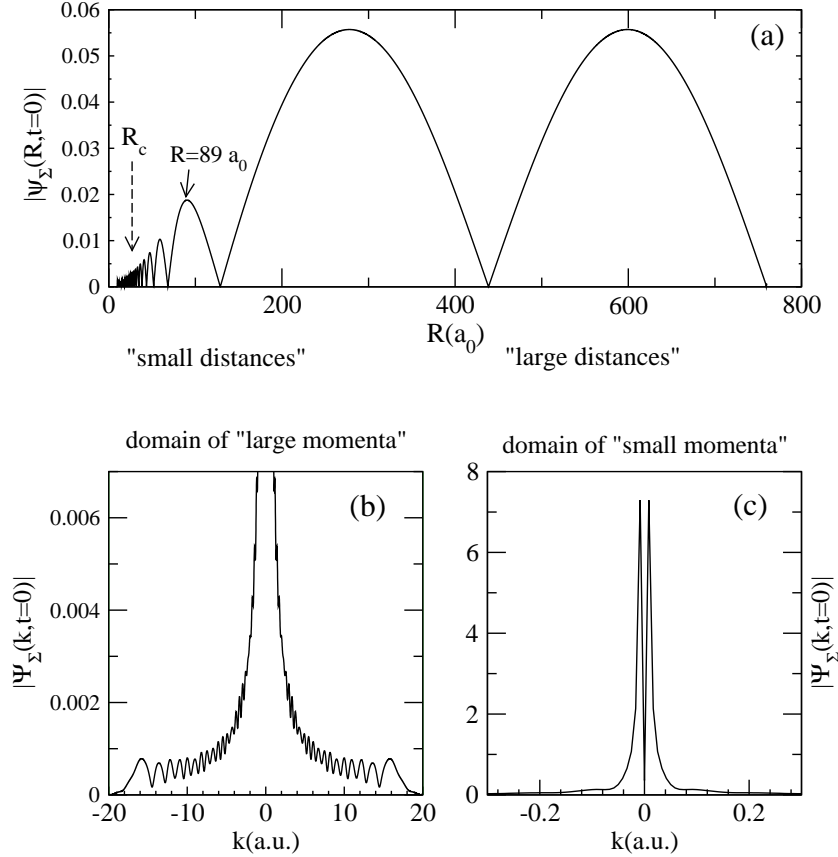


Figure 3. Initial state of the photoassociation process of energy E_0 : stationary continuum state in the $a^3\Sigma_u^+$ potential, calculated and normalized to 1 in a box of length $L_R \approx 760$ a₀, corresponding to the temperature $E_0/k_B=0.11$ mK. (a) Position representation $|\Psi_\Sigma(R, 0)|$. (b) and (c) Momentum representation $|\Psi_\Sigma(k, 0)|$ shown in the domains of "large momenta" ($|k| < 20$ a.u.) and "small momenta" ($|k| < 0.2$ a.u.), respectively.

2.3. Initial state: spatial and momentum representations

The representation of the initial state in a wavepacket treatment of the cold atoms photoassociation is discussed in [10]. For a low temperature collision ($T = 0.11$ mK) and an excitation process taking place at short distances ($R_c = 29.3$ a₀), the initial state of the photoassociation process has to be represented using stationary collision states. We shall simulate the photoassociation dynamics using as initial state a continuum state of the ground electronic channel, having the energy $E_0 = k_B T$. The results obtained can be used to estimate a photoassociation probability for an ensemble of cold atoms in thermal equilibrium at temperature T (see Section 4).

In our numerical method, the initial continuum state is calculated as one of the eigenstates of the ground electronic state Hamiltonian, through the Sine Grid Representation [27], in a box of length L_R . The method introduces a discretization of the continuum which supply continuum states having a node at the boundary of

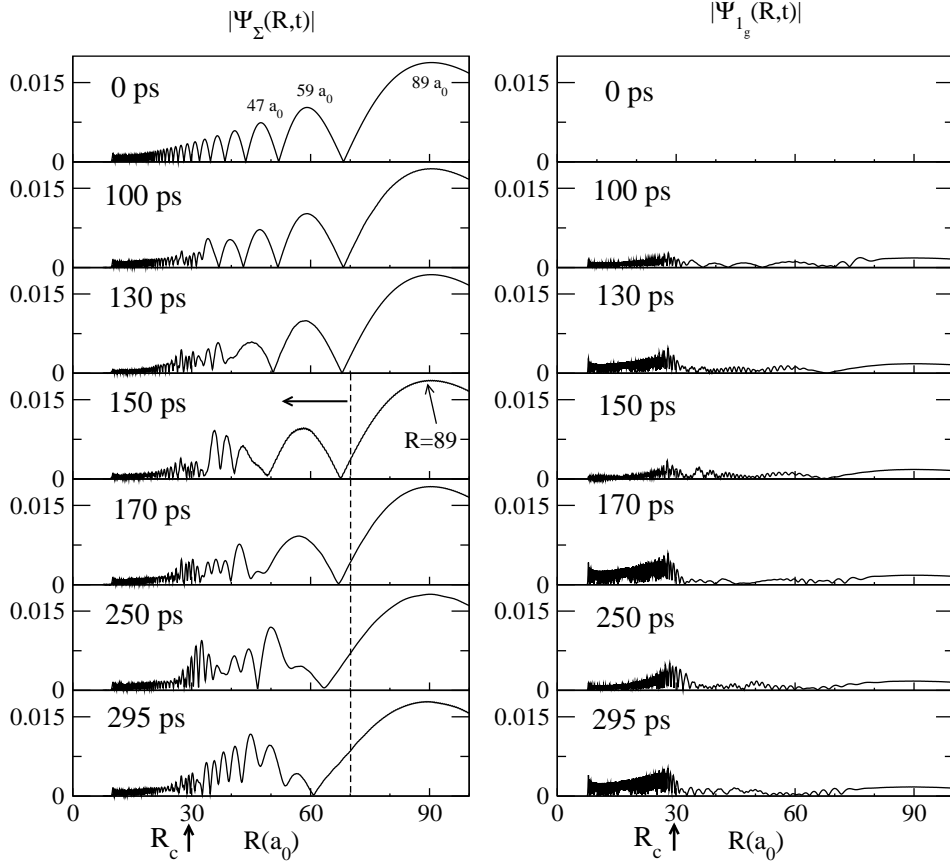


Figure 4. Time evolution of the wavepackets in the position representation: $|\Psi_\Sigma(R, t)|$ (left column) and $|\Psi_{1g}(R, t)|$ (right column). The vertical dashed line in the left column marks the part of the $a^3\Sigma_u^+$ wavepacket which is strongly accelerated inside the potential during the pulse.

the box (as the sine basis functions used in representation). Then it is possible to have a continuum delocalized state as initial state in the wavepackets simulation of the photoassociation dynamics. The MSG method allows the use of large spatial grids on which the wavepackets dynamics in the range of distances relevant for the problem can be followed for long propagation times without being influenced by the external boundary of the box [10].

Here the initial state $\Psi_\Sigma(R, 0)$ (see the (a) panel in figure 3) is chosen to be a continuum wavefunction of the $a^3\Sigma_u^+(6s, 6s)$ potential, of energy $E_0 = 7.6908 \times 10^{-3} \text{ cm}^{-1}$ corresponding to a temperature $T = E_0/k_B = 0.11 \text{ mK}$. This wavefunction is calculated through the MSG method [27, 10] in the box of length $L_R \approx 760 \text{ a}_0$, with a node at the end of the grid, and normalized to 1 on the grid. To obtain the normalization per unit energy the populations have to be multiplied by the density of states in the box at E_0 , $[(dE/dn)|_{E_0}]^{-1}$ [10]. The energy resolution for neighbouring eigenstates in the box at E_0 is $\delta E|_{E=E_0} = (dE/dn)|_{E_0} = 0.632 \times 10^{-4} \text{ cm}^{-1}$, corresponding to $[\delta E|_{E=E_0}]/k_B = 0.09 \text{ mK}$.

Figures 3(b) and (c) show the amplitude of the initial wavefunction in the

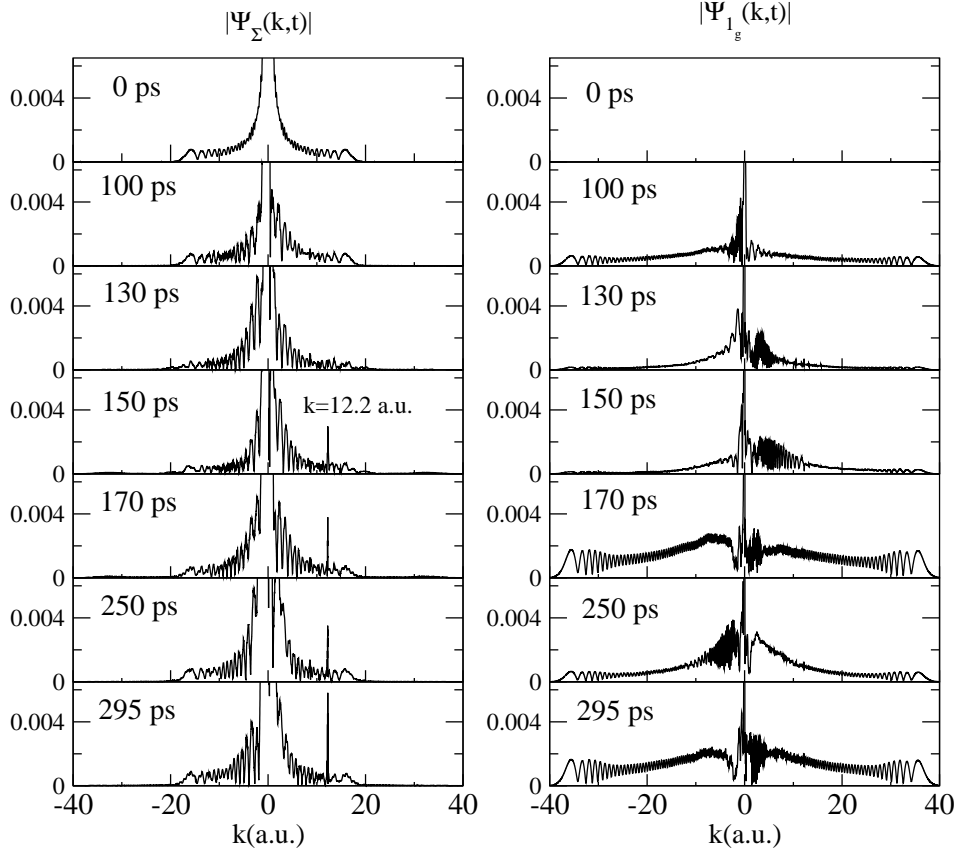


Figure 5. Time evolution of the wavepackets in the momentum representation $|\Psi_\Sigma(k, t)|$ (left column) and $|\Psi_{1g}(k, t)|$ (right column).

momentum representation, $|\Psi_\Sigma(k, 0)|$. The wavefunction amplitude is mainly localized in the domain of “small momenta”, $|k| < 0.06$ a.u. (figure 3(c)), which corresponds to the large distances domain ($R > 100$ a₀) in the position representation. A picture from the domain of “large momenta” ($|k| < 20$ a.u.), where the wavefunction amplitude is much smaller, is displayed in figure 3(b). This domain of momenta corresponds to the domain of “small distances” in figure 3(a). We are interested to observe the changes appearing in both domains during the time evolution. The negative k values mean momenta oriented to the inner wall of an electronic potential, and the positive k values momenta oriented to large distances.

2.4. Wavepackets evolution during the pulse: spatial and momentum representations

The evolution of the wavepackets during the pulse is illustrated in figures 4 and 5, showing the $a^3\Sigma_u^+$ and 1_g wavepackets in the spatial and momentum representations, respectively. The dynamics will be analysed in order to understand the vibrational movements inside each channel and the exchange of population between the electronic channels (figure 6).

In the 1_g potential, the excited wavepacket extends on the whole spatial grid,

showing that bound and continuum levels are populated *during the pulse*. The vibrational movement of the population occupying bound states with outer turning points in the crossing region ($R_c = 29.3 a_0$) can be well observed in the right columns of figures 4 and 5. The large amplitude of the wavepacket in the zone of big momenta ($t=170, 250, 295$ ps in the right column in figure 4) is equivalent with a strong presence of population at $R < R_c$ at the same moments. *After the pulse*, only bound levels remain populated in 1_g (figure 8 and section 4).

In the $a^3\Sigma_u^+$ potential, the wavepacket moves progressively to the inner region (left column of figure 4). The vertical line in the same figure marks the separation in two spatial domains, which are differently affected by the pulse: at small and intermediate distances $R < 70 a_0$, the wavepacket is accelerated and deformed, but at large interatomic separations $R > 80 a_0$ the action of the pulse can be considered as impulsive.

The wavepackets dynamics in the momentum representation (figure 5) makes visible an unexpected feature which appears from $t=150$ ps in the time evolution of the ground state wavepacket $\Psi_\Sigma(k, t)$ at $k \approx 12.2$ a.u., and whose intensity increases until the end of the pulse. This result will be analysed in section 4.3.

3. Analysis of the population transfer during the pulse

We shall analyse the time evolution of the population transferred by the pulse in the excited state, $P_{1_g}(t)$, calculated with formula (3) and displayed in figure 6 (the population in the ground state has a complementary evolution, as $P_\Sigma(t) + P_{1_g}(t) = 1$, with $P_\Sigma(0) = 1$). The figure shows that from the large amount of population $P_{1_g}(t)$ transferred during the pulse, which is of the order of 8.7×10^{-3} , only 7.77×10^{-5} remains at the end of the pulse. As it was discussed in the previous section, the large population transfer in the excited state during the pulse is related to the occupation of continuum states at large distances, in levels which do not rest populated after the pulse [9, 10]. On the contrary, what it is interesting for us is the population in bound vibrational levels, counting as cold molecules formation.

The vibrational levels of 1_g and $a^3\Sigma_u^+$ predominantly populated by the pulse were identified by calculating the probabilities $P_{v_e, v_g}(t) = | \langle \Psi_{e,g}(R, t) | \chi_{v_e, v_g}(R) \rangle |^2$ that a certain vibrational level of the excited or ground electronic state (v_e or v_g) to be populated at an instant t . Two kinds of bound vibrational levels are mainly populated during the pulse in the 1_g state:

- levels around the crossing of the diabatic potentials: $v_e=141-144$, with vibrational energies $E_{v_e} = -144.5, -141.39, -138.29, -135.24 \text{ cm}^{-1}$, lying in a domain of about 10 cm^{-1} containing the crossing energy $V_c = -143 \text{ cm}^{-1}$, and with outer turning points of the vibrational wavefunctions lying around $R_c = 29.3 a_0$. These levels have vibrational periods of about 11 ps (see table 1).
- levels with $v_e \geq 241$ ($E_{v_e=241} = -8.818 \text{ cm}^{-1}$), having vibrational wavefunctions lying at much larger distances ($R > 60 a_0$). From these levels populated at large

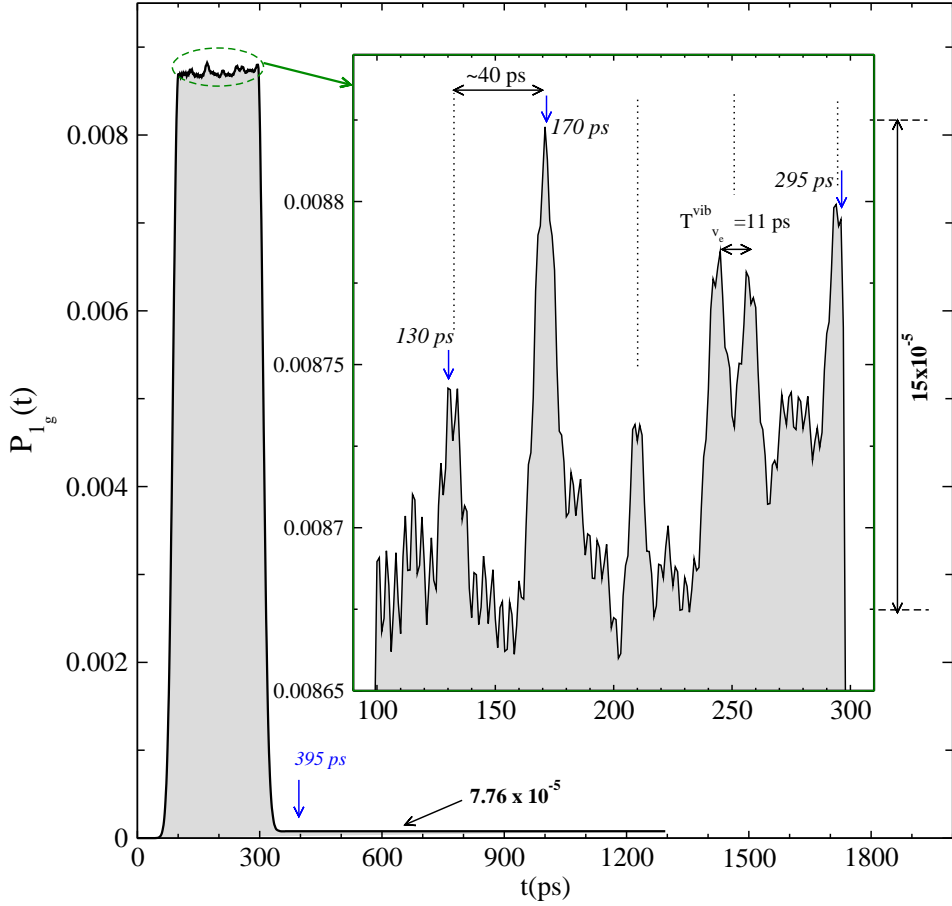


Figure 6. Time evolution of the population in the excited state, $P_{1g}(t)$, in the photoassociation with the pulse $W_L f(t)$ (whose envelope $f(t)$ is represented in figure 2). The inset shows the details of the time evolution during the constant coupling W_L (between 100 ps and 295 ps).

distances, only the levels $v_e = 244$ up to 248 remain notably populated after the pulse. Their vibrational periods are in the range 116 up to 130 ps.

The inset of figure 6 shows the evolution of $P_{1g}(t)$ in the time interval of constant coupling W_L (between 100 ps and 295 ps). The oscillating features of $P_{1g}(t)$ during this time interval come from the exchange of population between vibrational levels of 1_g and $a^3\Sigma_u^+$ located around the crossing ($v_e=141$ up to 144 in the excited state, and $v_g=44$ up to 49 in the ground state, see table 1), without major contribution from the population transferred at large distances. Indeed, as it is marked on the inset of figure 6, the energy domain covered by these oscillations is about 15×10^{-5} , comparable with the final population $P_{1g}(t = 395ps) = 7.77 \times 10^{-5}$ in bound levels. Also, the variations of the total population $P_{1g}(t)$ between instants as $t=130, 150, 170$ ps, etc. are very closed to the variations of the population in levels around the crossing, given by the sum $P_{1g}^{141-144}(t) = \sum_{v_e=141}^{144} P_{v_e}(t)$. Comparatively, the probability for the population of the levels $v_e=244-248$, $P_{1g}^{244-248}(t) = \sum_{v_e=244}^{248} P_{v_e}(t)$, shows much smaller variations.

The quantum beats appearing in figure 6 are related to the characteristic times

Table 1. Vibrational levels v_e of the excited state (with energies E_{v_e} and vibrational periods $T_{v_e}^{vib}$) and v_g of the ground state (with energies E_{v_g} and vibrational periods $T_{v_g}^{vib}$), populated during the pulse and giving the quantum beats shown in the inset of figure 6. $\{v_e\}$ are 1_g vibrational levels located around the crossing of the diabatic potentials and $\{v_g\}$ are vibrational levels in the $a^3\Sigma_u^+$ potential giving the biggest overlaps $\langle \chi_{v_g} | \chi_{v_e} \rangle$ with every v_e level. The last two columns show the energy differences $|E_{v_g} - E_{v_e}|$ and the characteristic times T_{v_g, v_e}^L , calculated with formula (10). The energy origin is the dissociation limit $E_{6s+6p_{3/2}}$ of the $1_g(6s, 6p_{3/2})$ potential.

v_e	$T_{v_e}^{vib}$ (ps)	E_{v_e} (cm $^{-1}$)	v_g	$T_{v_g}^{vib}$ (ps)	E_{v_g} (cm $^{-1}$)	$\langle \chi_{v_g} \chi_{v_e} \rangle$	$ E_{v_g} - E_{v_e} $ (cm $^{-1}$)	T_{v_e, v_g}^L (ps)
141	10.6	-144.05	44	40	-143.27	0.10	0.78	12.7
			45	49	-142.43	0.22	1.62	5.5
			46	62	-141.75	0.16	2.30	7
			47	80	-141.21	0.13	2.84	7.5
142	10.8	-140.90	44	40	-143.27	0.08	2.37	10.5
			45	49	-142.43	0.20	1.53	6
			46	62	-141.75	0.19	0.85	6.6
			49	155	-140.48	0.10	0.42	12.5
143	11	-137.81	44	40	-143.27	0.06	5.46	9
			45	49	-142.43	0.19	4.62	4.5
			46	62	-141.75	0.22	3.94	4.8
			49	155	-140.48	0.11	2.67	8.5
144	11.1	-134.77	44	40	-143.27	0.05	8.50	3.9
			45	49	-142.43	0.17	7.66	3.8
			46	62	-141.75	0.23	6.98	2.5
			48	108	-140.79	0.12	6.02	5

of the dynamics: the vibrational movement in each potential well and the beating between the two coupled wavepackets, which are superpositions of vibrational functions corresponding to each electronic potential, as in (6) and (7). Table 1 gives a list of energies E_v , vibrational periods T^{vib} , and characteristic beating times T_{v_g, v_e}^L between levels in the ground and excited electronic states which contribute significantly in the exchange of populations between the two coupled channels; it also contains the overlaps $\langle \chi_{v_g} | \chi_{v_e} \rangle$ with $a^3\Sigma_u^+$ levels. Only the v_g levels having the biggest overlaps with a given v_e level are shown: these are the levels $v_g=44$ up to 49, whose vibrational wavefunctions have the outer turning points at distances $R < 35 a_0$ in the $a^3\Sigma_u^+$ potential, and which are strongly populated by the pulse.

The population transfer between the two electronic channels is regulated by two time scales: a longer one, related to the vibrational movements inside the potential wells, and a shorter one, related to the Rabi coupling. The longer scale reflects the influence of the vibrational movements on the exchange of population between the two channels: the exchange is maximal when the amplitudes of the two wavepackets have a significant overlap, which, in the case of wavepackets vibrating in two different potential wells,

arrives when both wavepackets have important localization probabilities in the crossing region [18]. When one of the wavepackets vibrates inside its potential, the transfer is generally diminished. The levels in the ground state have vibrational periods (> 40 ps) much longer than the levels in the excited state (about 11 ps). This explains the period of 40 ps appearing in the $P_{1g}(t)$ oscillations, which coincides with the vibrational period of the level $v_g=44$ in the $a^3\Sigma_u^+$ ground state, whose energy -143.27 cm $^{-1}$ is very close to the crossing energy V_c . On a much shorter scale, the transfer is guided by the strong laser coupling, which couples differently the implied levels. Table 1 shows characteristic times T_{v_g, v_e}^L of beating (calculated with formula 10) varying from 2.5 to 12.7 ps for coupled pairs of vibrational levels in the ground and excited states. Comparing these times with the vibrational periods of the concerned levels, the strength of the coupling appears as varying very much among pairs of levels. The times scales given by T_{v_g, v_e}^L are indicative for the short Rabi times appearing during the dynamics, for example the periods of 3 up to 4 ps of the fast oscillations in $P_{1g}(t)$.

During the pulse the population accumulates in the 1_g state, such as in figure 6 appear not only the population beatings between the two channels, but also traces of the vibrational dynamics inside the excited potential: around $t=250$ ps, the two peaks of $P_{1g}(t)$ are separated by a time interval of ≈ 11 ps, which is the vibrational period of the $v_e = 142, 143$ levels located around the crossing: $T_{v_e=142,143}^{vib} \approx 11$ ps.

3.1. The light-induced (adiabatic) potentials

The mechanism of the population transfer during the pulse is enlightened if one analyses the light-induced (adiabatic) potentials. In figure 1 are represented both the diabatic potentials $V_{1g, \Sigma}(R)$ and the adiabatic ones, V_{ad}^e and V_{ad}^g , obtained from the diagonalization of the 2x2 potential matrix $\hat{\mathbf{V}}_{el}$ with constant coupling $\hat{\mathbf{W}}_L$ as non-diagonal term:

$$(\hat{\mathbf{V}}_{el} + \hat{\mathbf{W}}_L)|_{diab} = \begin{pmatrix} V_{1g}(R) & W_L \\ W_L & V_{\Sigma}(R) \end{pmatrix} \quad (12)$$

$$(\hat{\mathbf{V}}_{el} + \hat{\mathbf{W}}_L)|_{adiab} = \begin{pmatrix} V_{ad}^e(R) & 0 \\ 0 & V_{ad}^g(R) \end{pmatrix} \quad (13)$$

Expressions (12) and (13) illustrate the diabatic and adiabatic representations, respectively, of the $\hat{\mathbf{V}}_{el} + \hat{\mathbf{W}}_L$ operator. The coupling produces a strong deformation of the diabatic potentials V_{1g}, V_{Σ} around the crossing (figure 1), but its influence goes far beyond the crossing region, and this can be clearly seen if one compares the vibrational levels of the diabatic potentials V_{1g}, V_{Σ} with those of the adiabatic ones V_{ad}^e, V_{ad}^g . Such a comparison can be made using the series of rotational constants $B_v = \langle \chi_v | \hbar^2 / (2\mu R^2) | \chi_v \rangle$ characterizing every potential. The energies E_v and rotational constants B_v were computed by solving numerically the corresponding stationnary Schrödinger equation $(\hat{\mathbf{T}} + \hat{\mathbf{V}})|\chi_v\rangle = E_v|\chi_v\rangle$ using the Mapped Fourier Grid Hamiltonian (MFGH) method [26]. In figure 7 are represented the rotational constants B_v as functions of the

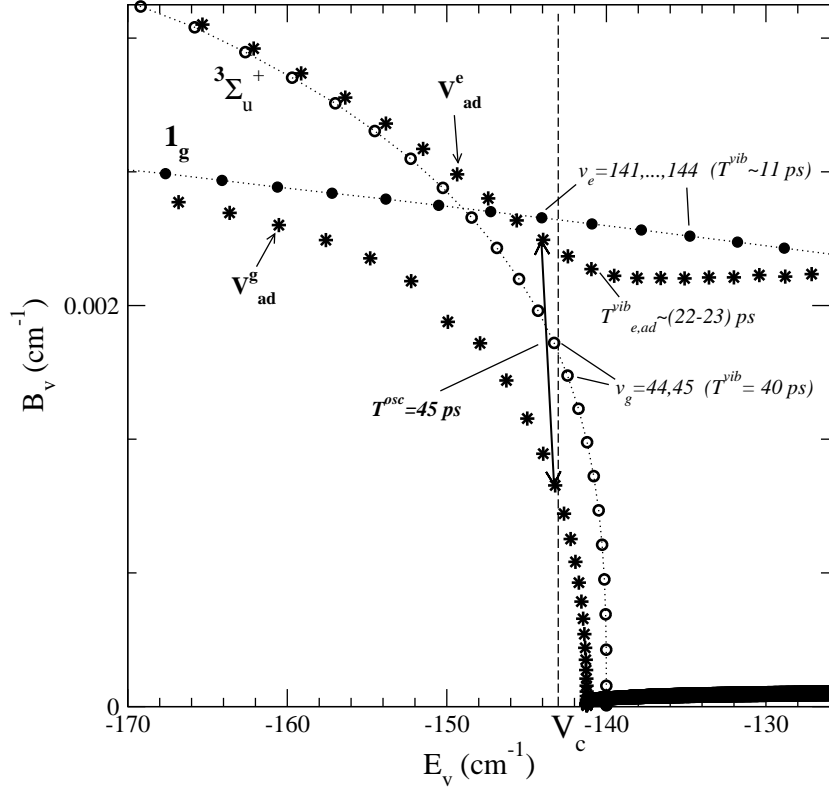


Figure 7. Rotational constants $B_v = \langle \chi_v | \hbar^2 / (2\mu R^2) | \chi_v \rangle$ as functions of the vibrational energies E_v , for vibrational levels of the 1_g and $a^3\Sigma_u^+$ diabatic potentials (full and empty circles, respectively), and of the adiabatic potentials V_{ad}^g , V_{ad}^e (stars). The vertical line at $V_c = -143 \text{ cm}^{-1}$ indicates the crossing region.

vibrational energies E_v for $a^3\Sigma_u^+$ and 1_g diabatic potentials, as well as for the adiabatic potentials V_{ad}^e , V_{ad}^g . We use the $B_v(E_v)$ functions to observe how the energies of the vibrational levels in these potentials are distributed in a domain lying between -170 and -128 cm^{-1} around the crossing energy $V_c = -143 \text{ cm}^{-1}$. These results show that the influence of the coupling is strongly felt in a large energy domain of several tens of cm^{-1} around the crossing.

Also marked in figure 7 are the vibrational levels populated during the pulse and relevant to the dynamics, together with their vibrational periods. We shall focus on the levels located around the crossing region. The levels $v_g = 44, 45$ in the $a^3\Sigma_u^+$ potential have vibrational periods $T_{v_g}^{\text{vib}} = 40, 49 \text{ ps}$. In the same energy region, the levels of the V_{ad}^g potential have bigger vibrational periods $T_{g,ad}^{\text{vib}} = 43, 58 \text{ ps}$. Also, if the vibrational period of the 1_g levels located around the crossing, $v_e = 141$ up to 144, is $T_{v_e}^{\text{vib}} \approx 11 \text{ ps}$, in the adiabatic potential V_{ad}^e the levels belonging to the same energy domain have a vibrational period twice bigger: $T_{e,ad}^{\text{vib}} \approx 23 \text{ ps}$. Then, as it could be expected from the shape of the V_{ad}^e and V_{ad}^g (figure 1), the vibration in the adiabatic potentials is slowed down in the crossing region, influencing the population transfer between the two channels. The slowing down of the vibrational movement in the excited state lead to longer periods for the population exchange between the two channels and constitutes a

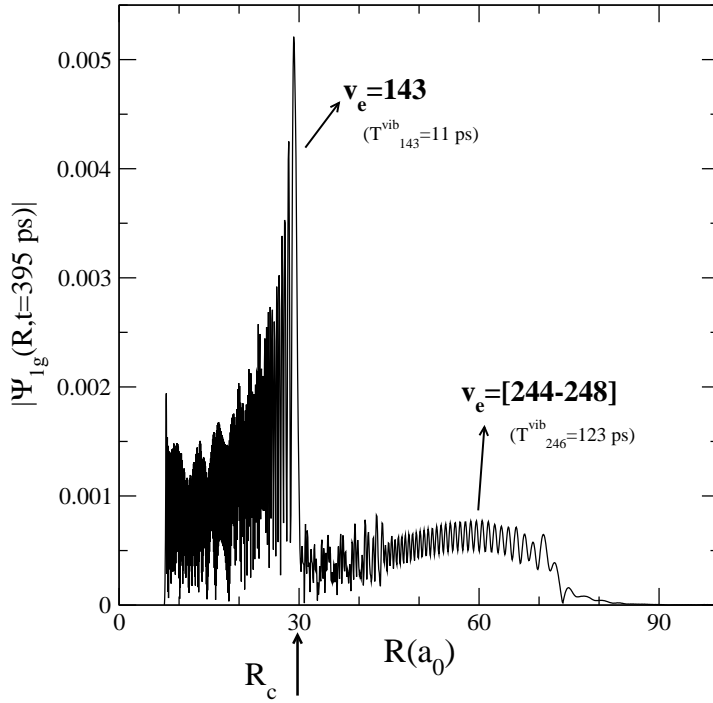


Figure 8. 1_g wavefunction at the end of the pulse.

mechanism for increasing progressively the population in the excited state.

The analysis of the adiabatic potentials can be used to extract characteristic times for the population exchange between the two channels. In an analogy with a two coupled states system, the Rabi beatings in the exchange of population is related to the Bohr frequency of the coupled system, which here can be found from the typical frequencies $|E_{ad}^e - E_{ad}^g|/2\hbar$, connected with the new energies E_{ad}^e , E_{ad}^g of the levels in the coupled system. In figure 7 we show that for levels located in the crossing region such a characteristic time $T_{osc} = 2\pi\hbar/|E_{ad}^e - E_{ad}^g|$ is about 45 ps, close to the period of ≈ 40 ps of the large oscillations in figure 6.

4. Results at the end of the pulse

Figures 8 and 9 show the wavepackets 1_g (in position representation) and $a^3\Sigma_u^+$ (in position and momentum representations) at the end of the pulse ($t=395$ ps). The main characteristics of the results will be discussed in the following.

4.1. Formation of strongly bound cold molecules in $a^3\Sigma_u^+$ and 1_g electronic states

The strong coupling between the ground and excited states creates an interesting result at the end of the pulse: the population in bound levels of the ground state (mainly six levels, $v_g = 47$ up to 52), $P_{\Sigma}^{47-52}(t=395 \text{ ps}) = 2.83 \times 10^{-4}$, is much bigger than the population photoassociated in the excited state, $P_{1_g}(t=395 \text{ ps}) = 0.78 \times 10^{-4}$. Some of the vibrational levels populated in $a^3\Sigma_u^+$, for example $v_g = 47, 48, 49$, have wavefunctions

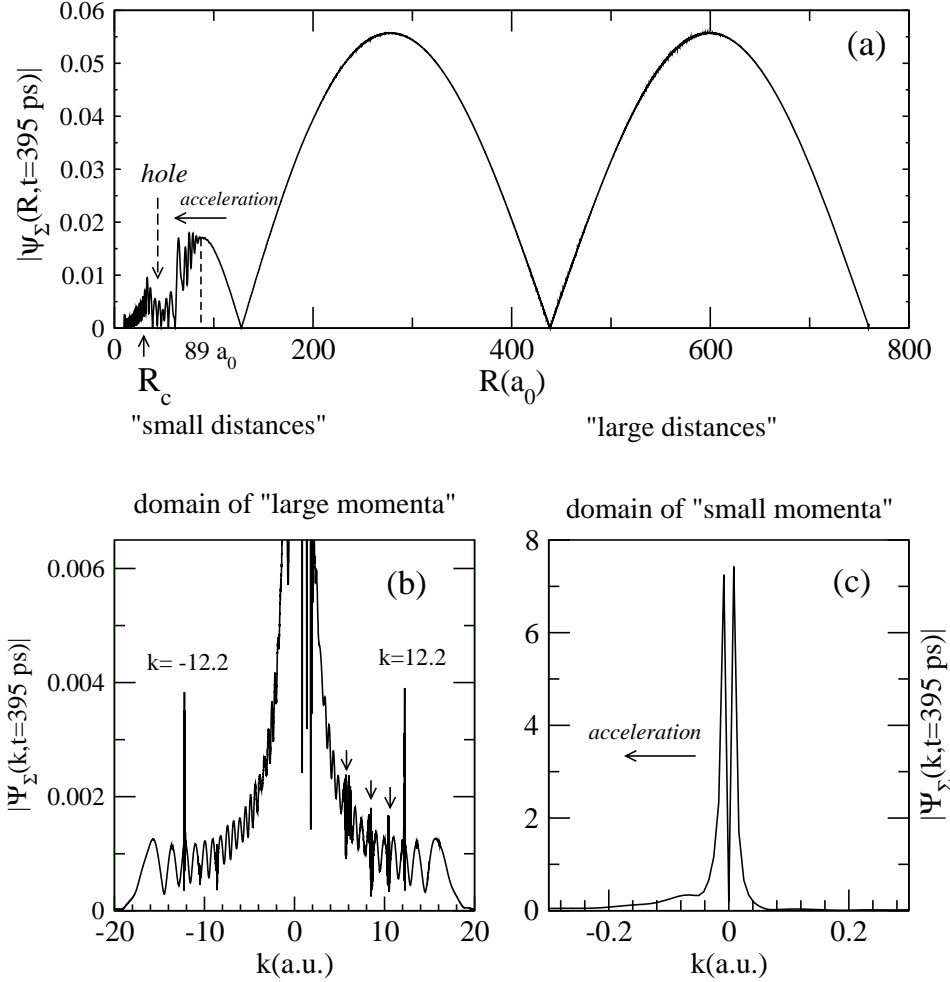


Figure 9. $a^3\Sigma_u^+$ wavepacket at the end of the pulse, $t=395$ ps. (a) Position representation $|\Psi_\Sigma(R, t=395 \text{ ps})|$. (b) and (c) Momentum representation $|\Psi_\Sigma(k, t=395 \text{ ps})|$ in the domain of "large momenta" ($|k| < 20 \text{ a.u.}$) and "small momenta" ($|k| < 0.2 \text{ a.u.}$), respectively.

localized at distances $R < 35 a_0$, being then strongly bounded.

The final population in the 1_g excited state (figure 8) is entirely in bound vibrational states. A superposition of two kinds of vibrational levels is created, showing two mechanisms in the population transfer: *at resonance*, where mainly one level rests populated, $v_e=143$ (with outer turning point at $\approx 30 a_0$), whose population represents 82% $P_{1_g}(t=395 \text{ ps})$, and *off-resonance* where several vibrational levels with outer turning points around $R \approx 70 a_0$ ($v_e=244$ up to 248, representing 15% $P_{1_g}(t=395 \text{ ps})$) are populated due to the strong coupling catching the large amplitude of the initial wavefunction between 45 and 65 a_0 (figure 10). This last kind of transfer creates a *hole in the ground state* in this domain of interatomic distances, as it is indicated in figures 9(a) and 10. Such a result reflects the specificity of the present photoassociation conditions of strong field and large detuning.

The results obtained for a total population normalized at 1 on the grid allow an

estimation of the averaged probability corresponding to a thermal distribution [10] at the temperature $T = E_0/k_B = 0.11$ mK, as:

$$P_{1g}(T) \approx P_{1g}(E_0) \left(\frac{dE}{dn} \big|_{E_0} \right)^{-1} \frac{k_B T}{Z} \quad (14)$$

where $P_{1g}(E_0) = P_{1g}(t=395 \text{ ps}) = 0.78 \times 10^{-4}$ is the 1_g probability obtained in the present calculation with an initial state of energy E_0 , $\left[(dE/dn) \big|_{E_0} \right]^{-1}$ is the density of states in the box of length L_R at E_0 , k_B is the Boltzmann constant, and Z is the partition function for a gas composed of non-interacting pairs of atoms in a volume V (with μ the reduced mass of the diatom): $Z = (2\pi\mu k_B T)^{3/2} V/h^3$. We then obtain $ZP_{1g}(0.11 \text{ mK}) = 0.95 \times 10^{-4}$ and $ZP_{\Sigma}^{v_g=47-52}(0.11 \text{ mK}) = 3.44 \times 10^{-4}$. For a number of N atoms in a volume V , and taking into account the spin degeneracy of the $Cs(6^2S)$ atomic state and of the initial electronic state, the total number of molecules photoassociated in 1_g per pump pulse is [10]: $N_{mol,1g} = \frac{N^2}{2} P_{1g}(T)^{\frac{3}{4}}$. For a volume $V=10^{-3} \text{ cm}^3$ and a density of atoms $N/V=10^{11} \text{ atoms/cm}^3$, the number of molecules obtained at the end of the pulse are: $N_{mol,1g} = 0.3 \times 10^{-2}$ and $N_{mol,\Sigma,v_g=47-52} = 1.1 \times 10^{-2}$.

4.2. Acceleration of the $a^3\Sigma_u^+$ wavepacket to small interatomic distances

During the pulse, the $a^3\Sigma_u^+$ slow packet is accelerated towards small interatomic distances R . The left column of figure 4 shows the time evolution of the $a^3\Sigma_u^+$ wavepacket, which advances progressively to the inner zone. Especially the part of the wavepacket occupying distances $R < 70 \text{ a}_0$ feels the acceleration to the crossing zone, where the diabatic potential $a^3\Sigma_u^+$ in R^{-6} becomes the adiabatic one V_{ad}^g decreasing in R^{-3} (see figure 1). On the contrary, the maximum of the wavefunction located at $R \approx 89 \text{ a}_0$ does not move during the pulse, but begin to be accelerated after the pulse. Similar observations can be made on figure 9 (a), showing the $a^3\Sigma_u^+$ R-wavepacket at the end of the pulse ($t=395 \text{ ps}$): the changes in the wavepacket amplitude are at distances $R < 89 \text{ a}_0$. The momentum representation of the $a^3\Sigma_u^+$ wavepacket at the same instant $t=395 \text{ ps}$, in figure 9 (c), shows that, compared with the initial symmetric distribution (figure 3 c), the part corresponding to $k < 0$ has moved to bigger $|k|$ values, which also indicates the gain of kinetic energy in the electronic potential in the movement to small distances.

The creation of a “hole” in the ground state wavepacket at the end of the pulse (discussed previously and shown in figure 9a)) is also a factor leading to a compression of population at short range, which after the pulse acts to increase the density of atom pairs at short distances [11].

4.3. Kinetic energy “gains” in the final $a^3\Sigma_u^+$ wavepacket as signatures of the maxima in the initial wavefunction continuum

In this section we shall analyse some peculiar features appearing in the ground state wavepacket $|\Psi_{\Sigma}(k, t)|$ during the time evolution and at the end of the pulse (figure 9b)). The time evolution in the momentum representation (left column of figure 5), shows

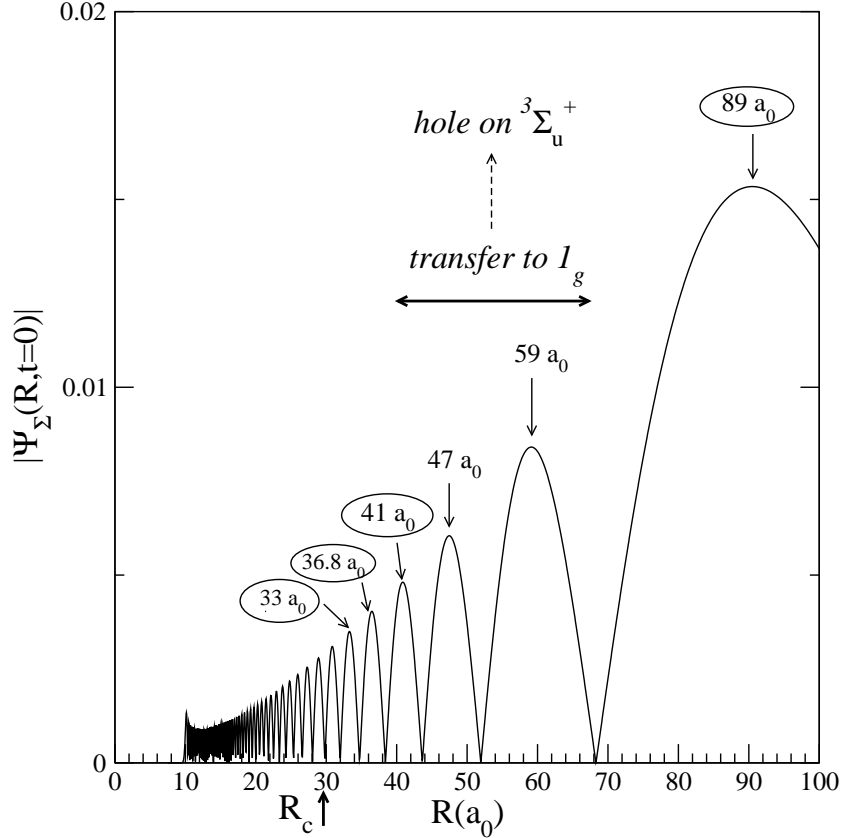


Figure 10. Details of the initial wavefunction on the ground state, $|\Psi_\Sigma(R, t = 0)|$. The arrows show local maxima of the wavefunction. The encircled ones give contributions to the off-resonance cycling of population between the two channels, bringing momentum to the final ground state wavepacket. On the contrary, ground state population from the local maxima at $R = 47$ a_0 and 59 a_0 is transferred to the excited state 1_g (figure 8), creating a hole in the final $a^3\Sigma_u^+$ wavepacket (figure 9a).

that, from $t=150$ ps, a line strikingly appears in the wavepacket amplitude $|\Psi_\Sigma(k, t)|$, at $k \approx 12.2$ a.u. The kinetic energy associated with this momentum is $\hbar^2 k^2 / 2\mu = 134.8$ $\text{cm}^{-1} = |V_{1_g}(R) - V_\Sigma(R)|_{R=89a_0}$, corresponding to the local difference in energy between $V_{1_g}(R)$ and $V_\Sigma(R)$ potentials at $R = 89$ a_0 . The amplitude of the initial wavefunction $|\Psi_\Sigma(R, 0)|$ has a maximum at this distance (figure 3 a), which does not move during the time evolution, but on which small oscillations begin to be superposed (see the left column of figure 4). The period of these oscillations is $T_R = 0.5$ $a_0 = 2\pi/k$, corresponding to a plane wave $\exp(ikR)$ with $k = 12.2$ a.u. The momentum width of this k -feature in the $|\Psi_\Sigma(k, t)|$ wavepacket is $\Delta k \approx 0.15$ a.u., which is consistent with the spread in distance $\Delta R \geq 3.3$ a_0 on $|\Psi_\Sigma(R, t)|$ around $R \approx 89$ a_0 . We interpret this feature as corresponding to the kinetic energy of the population cycled back in the ground state from the excited state in the fast exchange of populations taking place around $R \approx 89$ a_0 due to the strong coupling between the two electronic channels, with $T_{Rabi}^L(89 a_0) = 0.24$ ps. At the end of the pulse, the line with $k \approx 12.2$ a.u. is accompanied in the $|\Psi_\Sigma(k, t = 395 \text{ ps})|$ wavepacket by its negative value $k = -12.2$ a.u.

(see figure 9b), which has to be a technical artefact coming from the propagation of this large positive momentum component to large interatomic R distances, followed by reflection at the end of the grid.

In fact, as it is shown in the Appendix, it seems that the momentum k first appears associated with an ingoing plane wave travelling to small distances ($k < 0$), but it is fast reflected by the inner wall of the potential and transformed in a positive k travelling to large distances, which is easy to be observed in the wavepackets evolution. We have simulated the dynamics in the same conditions, but taking as initial wavepacket in the ground state a gaussian centered at $R = 89 a_0$, and indeed we observed a peak at $k = -12.2$ a.u. appearing early in the time evolution.

$k = 12.2$ a.u. is not the only value of momentum for which a feature appears in the $|\Psi_\Sigma(k, t)|$ wavepacket. At various instants of the time evolution, other lines can be observed, at smaller values of k . As these lines are embedded in the wavepacket, it becomes easier to distinguish them for larger momenta where the wavefunction amplitude is smaller. In figure 9b, showing the $a^3\Sigma_u^+$ wavepacket amplitude in the domain of large momenta, at the end of the pulse, other lines can be observed at the values: $k=12.2, 10.4, 8.6$ and 6 a.u. They correspond to kinetic energies $\hbar^2 k^2 / 2\mu = 134.8, 98, 68.6$ and 32.6 cm $^{-1}$. If one associates these kinetic energies to local differences $\Delta V(R)$ between the electronic potentials, then, according to the reasoning just exposed they correspond to local transitions from the excited to the ground state taking place at distances $R \approx 89, 43.9, 36.8$ and $32 a_0$, where maxima of the initial wavefunction are located, as it appears in figure 10. Other local maxima of the initial wavefunction, at $R=47 a_0$ and $59 a_0$, do not have a correspondent k -value in the final momentum distribution of the ground state wavepacket, but in this domain of distances the population is not cycled back to the ground state, remaining transferred to the levels $v_e=244$ up to 248 of the excited state (see figure 8). As a consequence, as we showed already, a hole is created in the ground state in this spatial domain (figure 9a).

We also have to mention that for longer propagation times one can see appearing in the $|\Psi_\Sigma(k, t)|$ wavepacket peaks corresponding to the negative k values of these other smaller momenta: $-10.4, -8.6$ and -6 a.u.

In the Appendix we use the impulsive approximation in the limit $\Delta(R) \gg W_L$ to show the emergence of such momenta during the time evolution. Indeed, as we emphasized, for the maximum of the ground wavefunction located at $R = 89 a_0$, the impulsive approximation rests valid during the whole pulse (see figure 9a), and for other maxima the impulsive approximation could be applied on smaller durations of the pulse.

The significant fact is that these “large momenta” appearing at the end of the pulse in the ground state wavepacket are signatures of the maxima in the initial wavefunction continuum. This is a specific effect of the strong photoassociation pulse applied at small distances which reveals the structure of the initial ground state.

5. Comments and Conclusions

We have analysed the dynamics in the photoassociation of a pair of cold atoms by a strong laser pulse ($I \approx 43 \text{ MW/cm}^2$) applied at short interatomic distances ($R_c = 29.3 \text{ a}_0$) for a cold collision. The numerical calculations were made for the $a^3\Sigma_u^+(6s + 6s) \rightarrow 1_g(6s + 6p_{3/2})$ transition in Cs_2 , at a temperature $T = 0.11 \text{ mK}$. The large detuning ($\hbar\Delta_L = 140 \text{ cm}^{-1}$) and the intensity of the pulse were chosen to correspond to a specific regime imposed by the limit of an asymptotic detuning much bigger than the maximum of the coupling, $\hbar\Delta_L = 140 \text{ cm}^{-1} \gg W_L = 13.17 \text{ cm}^{-1}$, in order to avoid the transfer of population to the continuum of the excited state at the end of the pulse.

The specificity of this regime comes from two sides: a) the large detuning which locates the resonance condition at small or intermediate interatomic distances, making “visible” the nodal structure of the initial continuum wavefunction; b) the strong coupling between the two electronic channels, which acts not only on vibrational levels around the crossing of the dressed electronic potentials, but also induces off-resonance cyclings of population between the coupled electronic states.

We have chosen not only a quite strong pulse, but also a quite long one (a rectangular pulse of about 300 ps), in order to obtain a better understanding of the time evolution in the presence of the pulse and to see how efficient for the cold molecule formation is the acceleration of the population from large to small interatomic distances.

In this strong regime of coupling, the photoassociation dynamics during the pulse takes place in the light-induced (adiabatic) potentials, whose topology influence the exchange of population between the coupled channels. In our example, the shapes of the adiabatic potentials lead to acceleration of the ground state population to the inner region (at short distances the diabatic potential $a^3\Sigma_u^+$ in R^{-6} becomes the adiabatic one V_{ad}^g decreasing in R^{-3}), and also to the slowing down of the vibrational movement in the crossing region, which is a mechanism for increasing progressively the population in the excited state.

The main characteristics of the results at the end of the pulse are the following:

(i) It appears that such a pump scheme allows for the production of ground state molecules through a single laser pulse. Indeed, strongly bound cold molecules are formed in $a^3\Sigma_u^+$ and 1_g electronic states, the population transferred in bound levels of the ground state being much bigger than the population photoassociated in bound levels of the excited state. Some of the vibrational levels populated in $a^3\Sigma_u^+$ have wavefunctions localized at distances $R < 35 \text{ a}_0$. The final population in the 1_g excited state is entirely in bound vibrational levels, populated both at resonance ($v_e = 143$, with outer turning point at $\approx 30 \text{ a}_0$) and off-resonance, where several vibrational levels with outer turning points around $R \approx 70 \text{ a}_0$ are populated due to the strong coupling catching the large amplitude of the initial wavefunction between 45 and 65 a_0 . This last kind of transfer creates a *hole* in the ground state in this domain of interatomic distances.

(ii) During the pulse the population in the ground state is globally accelerated

towards small interatomic distances. The creation of a “hole” in the ground state wavepacket at the end of the pulse is also a factor leading to a compression of population at short distances [11].

(iii) At the end of the pulse, the momentum distribution of the ground state wavepacket keeps the traces of the initial continuum maxima. This is an effect of the strong coupling leading to off-resonance cycling of population between the two channels and bringing kinetic energy in the ground state. The cycling of population is particularly important at those interatomic distances where the maxima of the initial continuum are located.

An important question is if the regime explored here can be maintained if, for example, one increases the detuning $\hbar\Delta_L$, in order to form cold molecules in lower vibrational levels of the ground state. An insight about the results which can appear by increasing the detuning can be extracted in *the impulsive limit*, which normally rests valid at large interatomic separations. In the impulsive limit, the population in the excited state at the end of the pulse can be approximated as [24]:

$$|\Psi_e(R, t)|^2 \approx \frac{W_L^2}{W_L^2 + \Delta^2(R)} \sin^2(\Omega t) |\Psi_g(R, 0)|^2, \quad (15)$$

where $\hbar\Omega(R) = \sqrt{W_L^2 + \Delta^2(R)}$ (for $R \rightarrow \infty$, $2\Delta(R) \rightarrow \hbar\Delta_L$). Equation (15) shows that the transfer from the ground to the excited state is favoured: a) at large interatomic distances R , because $|\Psi_g(R, 0)|^2$ is the amplitude of an initial continuum wavefunction of low energy in the ground state; b) at resonance ($\Delta(R) = 0$); c) for a strong coupling W_L , when, depending on the ratio $W_L/\hbar\Delta_L$ and the pulse duration, various ranges of distances can be populated. It has to be observed that, increasing the detuning $\Delta(R)$, one increases Ω , so the oscillations in $\sin^2(\Omega t)$ with the period π/Ω will be very fast and produce an unstable regime of transfer, in which the result at the end of the pulse cannot be predicted. In this regime, the large distances and the continuum of the excited state can easily rest populated after the end of the pulse. The only manner to overcome these difficulties is to increase the coupling, which can break the impulsive limit and bring population to short distances. Then, the ratio $W_L/\hbar\Delta_L$ is indeed a significant parameter for the regime explored here, which can be maintained for a larger detuning only if the pulse intensity is also increased.

The acceleration of the population to the inner region and the efficiency in forming strongly bound cold molecules is related here to a *non-impulsive regime of coupling* brought at $R < 70 a_0$ by the strength and the time duration of the pulse.

These results have to be completed with a further investigation of the time evolution subsequent to the pulse. Also the model can be enriched by considering couplings with other electronic surfaces. Our work is a tentative to show that the photoassociation of cold atoms at small/intermediate distances with an intense laser pulse offers the possibility to explore cold molecules formation using the specific topologies of the light-induced potentials. Favorable conditions can be found taking into account the variety of electronic transitions in alkali dimers which can be controlled by the parameters of

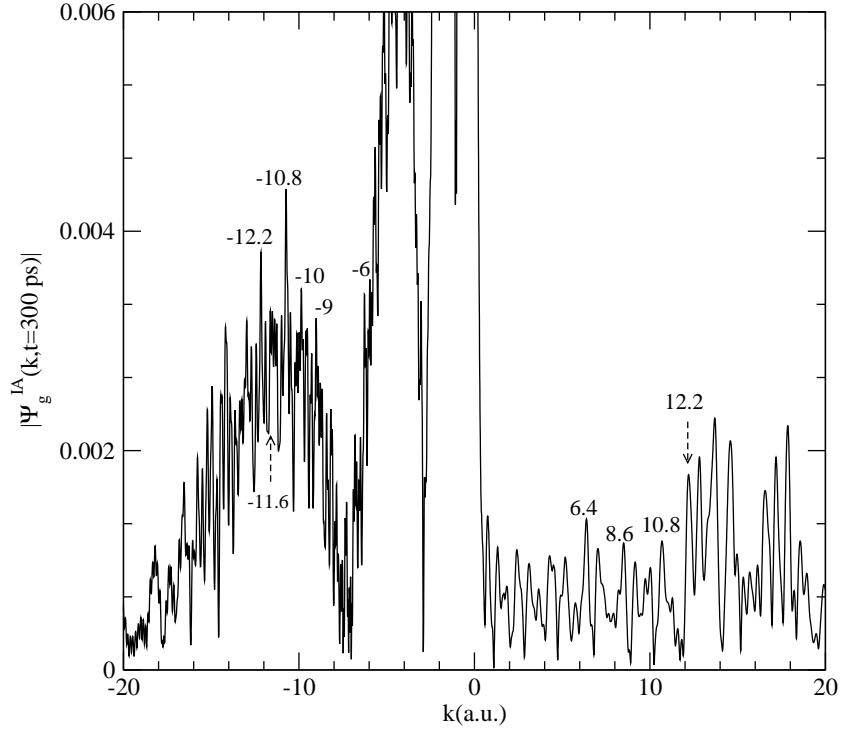


Figure A1. The momentum representation $|\Psi_g^{IA}(k, t = 300 \text{ ps})|$ of the wavefunction in the ground state $\Psi_g^{IA}(R, t)$, calculated in the impulsive approximation with (A.1), for $t=300 \text{ ps}$. The initial wavefunction $\Psi_g(R, 0)$ has maxima at $R = 33, 36.8, 41, 47, 59, 89 \text{ a}_0$ (see figure 10), which, according to our reasoning, are supposed to give peaks in the momentum distribution $\Psi_g^{IA}(k, t)$ of the ground state, at $k \approx 6, 8.6, 10.4, 10.8, 11.6, 12.2 \text{ a.u.}$ The figure shows that indeed the momentum distribution calculated in the impulsive approximation displays such peaks, at a time t close to the pulse duration. It can be noted that the amplitude of the $k = -12.2 \text{ a.u.}$ peak obtained here is close to 0.004, and that the same value can be observed in figure 9b) for $|\Psi_\Sigma(k = \pm 12.2 \text{ a.u.}, t = 395 \text{ ps})|$.

the photoassociation pulse.

Acknowledgments

Discussions with Prof. Ronnie Kosloff are gratefully acknowledged.

Appendix: Kinetic energy “gains” in the ground state due to the off-resonance cycling of population between the strongly coupled electronic states.

We shall consider the time-dependent Schrödinger equation (2) for constant coupling W_L . In [28] it is shown that, if the *impulsive approximation* is valid at a given R , the wavefunction on the ground state surface after a time t becomes:

$$\Psi_g^{IA}(R, t) = e^{-\frac{i}{\hbar}E_g t} e^{-\frac{i}{\hbar}\Delta t} \{ \cos(\Omega t) + i \cos \theta \sin(\Omega t) \} \Psi_g(R, 0), \quad (\text{A.1})$$

where E_g is the energy corresponding to the initial stationnary wavefunction at $t=0$ ($[T + V_g]\Psi_g(R, 0) = E_g\Psi_g(R, 0)$), $2\Delta(R) = |V_e(R) - V_g(R)|$ is the local detuning, $\Omega(R)$ the spatial dependent Rabi pulsation:

$$\hbar\Omega(R) = \sqrt{W_L^2 + \Delta(R)^2} \quad (\text{A.2})$$

and

$$\cos\theta(R) = \frac{\Delta(R)}{\hbar\Omega(R)} = \frac{\Delta(R)}{\sqrt{W_L^2 + \Delta(R)^2}}. \quad (\text{A.3})$$

We calculated numerically the time-dependent prediction for the ground state wavefunction in the impulsive approximation, $\Psi_g^{IA}(R, t)$, using (A.1). In figure A1 we show the corresponding momentum distribution at $t=300$ ps, $|\Psi_g^{IA}(k, t = 300 \text{ ps})|$, which indeed displays peaks at k values deduced from the maxima of the initial wavefunction, according to the discussion of Section 4.3.

In the following we shall introduce approximations into (A.1) in order to make appear analitically a momentum k associated with a maximum of the initial wavefunction at R_0 .

In (A.1), $e^{-\frac{i}{\hbar}E_g t}\Psi_g(R, 0)$ represents a free evolution in the ground state. The factor superposed on this free evolution can be separated:

$$A(R, t) = e^{-\frac{i}{\hbar}\Delta t}\{\cos(\Omega t) + i\cos\theta\sin(\Omega t)\} \quad (\text{A.4})$$

$$= \frac{1}{2}e^{i(\Omega - \frac{\Delta}{\hbar})t}(1 + \frac{\Delta}{\hbar\Omega}) + \frac{1}{2}e^{-i(\Omega + \frac{\Delta}{\hbar})t}(1 - \frac{\Delta}{\hbar\Omega}) \quad (\text{A.5})$$

We shall make approximations on the expression (A.5) in the limit $\Delta(R) \gg W_L$. Indeed, this limit is valid at $R_0 = 89 a_0$, where $\Delta(R_0) = \hbar\Delta_L/2 \approx 70 \text{ cm}^{-1}$, and $W_L = 13.17 \text{ cm}^{-1}$. Then it is possible to approximate:

$$\hbar\Omega = \Delta\sqrt{1 + \frac{W_L^2}{\Delta^2}} \approx \Delta + \frac{W_L^2}{2\Delta}. \quad (\text{A.6})$$

Consequently, at a given R value where the impulsive approximation is valid, $\Psi_g(R, t)$ can be decomposed in two terms:

$$\Psi_g^{IA}(R, t) \approx \Psi_g^{(1)}(R, t) + \Psi_g^{(2)}(R, t) \quad (\text{A.7})$$

$$\Psi_g^{(1)}(R, t) = \frac{1}{2}(1 + \frac{\Delta}{\hbar\Omega})e^{\frac{i}{\hbar}\frac{W_L^2}{2\Delta}t}e^{-\frac{i}{\hbar}E_g t}\Psi_g(R, 0) \quad (\text{A.8})$$

$$\Psi_g^{(2)}(R, t) = \frac{W_L^2}{4(\hbar\Omega)\Delta}e^{-\frac{i}{\hbar}[2\Delta + \frac{W_L^2}{2\Delta}]t}e^{-\frac{i}{\hbar}E_g t}\Psi_g(R, 0) \quad (\text{A.9})$$

For $\Delta \gg W_L$ the first term is the dominant one. Indeed, a rough approximation $\hbar\Omega \approx \Delta$ implies $|\Psi_g^{(1)}(R, t)| \approx |\Psi_g(R, 0)|$, the second term having an incomparable smaller contribution ($\frac{W_L^2}{4(\hbar\Omega)\Delta}|_{89a_0} = 0.0087 \ll 1$). It is the second “small” term which offers the explanation for the “k- features” observed in our results. Its Fourier transform is:

$$\Psi_g^{(2)}(k, t) = \int dR e^{-ikR}\Psi_g^{(2)}(R, t) \quad (\text{A.10})$$

$$= e^{-\frac{i}{\hbar}E_g t} \int dR \frac{W_L^2}{4(\hbar\Omega)\Delta} e^{-i[\frac{E_g}{\hbar}\Delta t + kR]}\Psi_g(R, 0) \quad (\text{A.11})$$

with $E_{2\Delta} = 2\Delta + \frac{W^2}{2\Delta} \approx 2\Delta$. We shall take into account only the contribution at the integral coming from a small domain of R , D_R , around the point R_0 , assuming that on this domain $\Psi_g(R, 0)$ is a Gaussian of width δ_R centered in R_0 : $\Psi_g(R, 0)|_{R_0} \approx \Psi_g(R_0, 0) \exp[-(R - R_0)^2/\delta_R^2]$, and that $E_{2\Delta}(R)$ depends linearly on R near R_0 : $E_{2\Delta}(R) \approx E_{2\Delta}(R_0) + \frac{dE_{2\Delta}}{dR}|_{R_0}(R - R_0)$. Then:

$$\begin{aligned} \Psi_g^{(2)}(k, t)|_{R_0} &\approx e^{-\frac{i}{\hbar}E_g t} \frac{W_L^2}{4\hbar\Omega(R_0)\Delta(R_0)} \Psi_g(R_0, 0) e^{-i[\frac{E_{2\Delta}(R_0)}{\hbar}t + kR_0]} \\ &\times \int_{-\delta_R}^{\delta_R} dr e^{-i[\frac{1}{\hbar}\frac{dE_{2\Delta}}{dR}|_{R_0}t + k]r} e^{-r^2/\delta_R^2} \end{aligned} \quad (\text{A.12})$$

where $r = R - R_0$ and the initial domain of integration was taken from $R_0 - \delta_R$ to $R_0 + \delta_R$. For a δ_R sufficiently large, the integral in (A.12) becomes a δ function, such as:

$$\begin{aligned} \Psi_g^{(2)}(k, t)|_{R_0} &\approx e^{-\frac{i}{\hbar}E_g t} \frac{W_L^2}{4\hbar\Omega(R_0)\Delta(R_0)} \Psi_g(R_0, 0) e^{-i[\frac{E_{2\Delta}(R_0)}{\hbar}t + kR_0]} \\ &\times 2\pi\delta(\frac{1}{\hbar}\frac{dE_{2\Delta}}{dR}|_{R_0}t + k) \end{aligned} \quad (\text{A.13})$$

In (A.13) one can see appearing the contribution of an ingoing ($kR_0 = -\vec{k}\vec{R}_0$) plane wave $e^{-i[\frac{E_{2\Delta}(R_0)}{\hbar}t + kR_0]}$, of energy $E_{2\Delta}(R_0)/\hbar$ and momentum $p = \hbar k$ [29]. The δ function shows that this momentum $p = \hbar k = -\frac{dE_{2\Delta}}{dR}|_{R_0}t$ is related to the local energy difference between the electronic potentials at R_0 , or that $dp/dt = -\frac{dE_{2\Delta}}{dR}|_{R_0}$. If one associates this momentum to the movement of an ingoing particle of mass μ , $p = -\mu dR/dt$, then one obtains $p/\mu = dE_{2\Delta}/dp$, and finally $E_{2\Delta} = p^2/2\mu$.

Then indeed (A.13) makes appear a momentum k connected to $2\Delta(R_0)$, as we observed in our results discussed in Section 4.3, and oriented to small R distances. The fact that we first observe an outgoing wave has to be due to the rapid reflection of the ingoing waves by the inner wall of the ground state potential.

An estimation of the wavefunction amplitude $\Psi_g^{(2)}(k, t)|_{R_0}$ for $R_0 = 89 a_0$ using formula (A.13) gives $|\Psi_g^{(2)}(k, t)|_{R_0=89a_0} \approx 0.001 \times \delta(\frac{1}{\hbar}\frac{dE_{2\Delta}}{dR}|_{R_0}t + k)$. This qualitative estimation obtained analitically for unprecised t corresponds to the amplitudes calculated numerically for $k = \pm 12.2$ a.u., from the dynamics and in the impulsive approximation, which are in agreement: $|\Psi_\Sigma(k = \pm 12.2 \text{ a.u.}, t = 395 \text{ ps})| \approx |\Psi_g^{IA}(k = -12.2 \text{ a.u.}, t = 300 \text{ ps})| \approx 0.004$ (see figure 9b) and figure A1).

References

- [1] Jones K M, Tiesinga E, Lett P D and Julienne P S 2006 *Rev. Mod. Phys.* **78** 483
- [2] Salzmann W *et al.* 2006 *Phys. Rev. A* **73** 023414
- [3] Brown B L, Dicks A J and Walmsley I A 2006 *Phys. Rev. Lett.* **96** 173002
- [4] Wright M J, Pechkis J A, Carini J L and Gould P L 2006, *Phys. Rev. A* **74** 063402
- [5] Wright M J, Pechkis J A, Carini J L, Kallush S, Kosloff R and Gould P L 2007 *Phys. Rev. A* **75** 051401(R)
- [6] Veshapidze G, Trachy M L, Jang H U, Fehrenbach C W and DePaola B D 2007 *Phys. Rev. A* **76** 051401(R)

- [7] Weise F *et al.* 2007 *Phys. Rev. A* **76** 063404
- [8] Vala J, Dulieu O, Masnou-Seeuws F, Pillet P and Kosloff R 2001 *Phys. Rev. A* **63** 013412
- [9] Luc-Koenig E, Kosloff R, Masnou-Seeuws F and Vatasescu M 2004 *Phys. Rev. A* **70** 033414
- [10] Luc-Koenig E, Vatasescu M and Masnou-Seeuws F 2004 *Eur. Phys. J. D.* **31** 239
- [11] Luc-Koenig E, Masnou-Seeuws F, and Kosloff R 2007 *Phys. Rev. A* **76** 053415
- [12] Koch C P, Luc-Koenig E and Masnou-Seeuws F 2006 *Phys. Rev. A* **73** 033408
- [13] Koch C P, Kosloff R and Masnou-Seeuws F 2006 *Phys. Rev. A* **73** 043409
- [14] Mur-Petit J, Luc-Koenig E and Masnou-Seeuws F 2007 *Phys. Rev. A* **75** 061404(R)
- [15] Kallush S and Kosloff R 2007 *Phys. Rev. A* **76** 053408
- [16] Shapiro E A, Shapiro M, Pe'er A and Ye J 2007, *Phys. Rev. A* **75** 013405
- [17] Shapiro E A, Pe'er A, Ye J, and Shapiro M 2008 *Phys. Rev. Lett.* **101** 023601
- [18] Vatasescu M, Dulieu O, Kosloff R, and Masnou-Seeuws F 2001 *Phys. Rev. A* **73** 033407
- [19] Vatasescu M 2008 *Nucl. Instr. and Meth. in Phys. Res. B* doi:10.1016/j.nimb.2008.10.033
- [20] Spies N 1989 *Ph.D. Thesis* Universität Kaiserslautern
- [21] Marinescu M and Dalgarno A 1995 *Phys. Rev. A* **52** 311
- [22] Marinescu M and Dalgarno A 1996 *Z. Phys. D* **36** 239
- [23] Vatasescu M 1999 *Ph. D. Thesis* Université Paris XI
- [24] Kosloff R 1994 *Annu. Rev. Phys. Chem.* **45** 145
- [25] Kosloff R 1996 Quantum Molecular Dynamics on Grids *Dynamics of Molecules and Chemical Reactions* ed R E Wyatt and J Z Zhang (New York: Marcel Dekker) pp 185-230
- [26] Kokoouline V, Dulieu O, Kosloff R and Masnou-Seeuws F 1999 *J. Chem. Phys.* **110** 9865
- [27] Willner K, Dulieu O and Masnou-Seeuws F 2004 *J. Chem. Phys.* **120** 548
- [28] Banin U, Bartana A, Ruhman S and Kosloff R 1994 *J. Chem. Phys.* **101** 8461
- [29] Messiah A 1969, *Mécanique Quantique* (vol 1) (Paris: Dunod)